Parametric studies on the water impact of one and twin free-falling wedges by a Cartesian grid multiphase flow model

Xin, Jianjian; Shi, Fulong; Fan, Shi; Jin, Qiu; Chang, Xing

Important note
To cite this publication, please use the final published version (if applicable).
Please check the document version above.

Parametric studies on the water impact of one and twin free-falling wedges by a Cartesian grid multiphase flow model

Jianjian Xin [a,b,*], Fulong Shi [c,**], Shi Fan [a,b], Qiu Jin [d], Xing Chang [e]

[a] Institute of Naval Architecture and Ocean Engineering, Ningbo University, Ningbo, 315211, China
[b] Jiangsu Province Collaborative Innovation Center of Modern Urban, Traffic Technologies, Southeast University, Road #2, Nanjing, 211189, PR China
[c] School of Shipping and Naval Arechitecture, Chongqing Jiaotong University, Chongqing, 400074, China
[d] Faculty of Engineering and the Environment, University of Southampton, Southampton, SO167QF, UK
[e] Section of Ship Hydro Mechanics, Delft University of Technology, 2628, CA, Delft, the Netherlands

ARTICLE INFO

ABSTRACT

The water impact of one and twin free-falling wedges is numerically investigated by a Cartesian grid multiphase flow model. The effects of the drop velocity and the gap distance on the hydrodynamic behaviors are parametrically investigated. The numerical model involves a radial basis function ghost cell method (RBFGCM) for treating moving bodies and a gradient-augmented level set method (GALS) method for capturing violent free surfaces. A case of twin wedges entering water is simulated to validate the accuracy of the present method. Good convergences are achieved. Then, the water entry of one and twin wedges in free falling is considered. The interaction mechanisms between twin wedges are discussed by comprehensively examining the variation patterns of the slamming load, the moment, the local pressure, and the fluid field. It is found that the second slamming load and the huge pressure pulse occur at the transition stage at narrow gap distances. The hydrodynamic interaction has more significant effects on the local pressure than that on the global load. In addition, distinct hydrodynamic phenomena for twin wedges entering water are observed such as the connection of the pressure contours, the extremely large jet flow, formation of the cavity, and even the ventilation.

1. Introduction

The water impact of multiple bodies is commonly encountered in the field of ocean engineering such as shuttle vessels connected to FPSO (Floating Production Storage and Offloading) for offloading operations, two parallel ships in replenishment, and two ships moored in close proximities. When two ships are parallelly moored in the harbor or in replenishment, they experience large-amplitude heave-rotation coupled motion under the effects of the wave and current. Each hull enters and exits the water continuously, which generates a huge impulsive load on each hull. The impulsive load can deteriorate the comfort of the crew and endanger the safety of the ship. Moreover, violent fluid motion between two ships can cause severe hydrodynamic interference, boosting the impulsive load in turn. The hydrodynamic interference can affect the ship maneuverability and seakeeping, which may yield ship collision or capsizal. Two adjacent ships in waves can be simplified as the water

entry of twin wedges. The results of twin wedges entering water are expected to aid in the safe operation of ship replenishment and offloading system.

Numerous studies have been conducted to predict the slamming load on a single body, including experimental, analytical and numerical methods in the past decades. Von Karman (1929) made pioneering work of predicting the impact load on a two-dimensional (2D) seaplane float by introducing the concept of added mass. Miloh (1991) studied a rigid sphere entering into an ideal incompressible fluid analytically through asymptotic small-time expressions. Recently, Sun et al. (2021) predicted the hydroelastic slamming loads of a 2D symmetric flexible body using the analytically modified Logvinovich model (MLM). However, analytical approaches are usually applied to the simple geometric body and the simplified model.

In the experimental studies, Aarsnes (1996) performed drop tests to study the water entry of a ship section for different roll angles. Wang

---

et al. (2015) investigated the water entry of a symmetric wedge experimentally. They categorized the water entry procedure into four successive stages: the slamming stage, the transition stage, the collapse stage, and the post-closure stage. Also, Derakhshanian et al. (2018) studied oblique water entry of bodies with blunt noses by a high-speed video camera. Shabani et al. (2019) investigated the slamming loads and pressures on high-speed catamarans in waves. Other recent experimental studies can be referred to (Xia et al., 2019; Xie et al., 2019; Duan et al., 2020). Although the experiments provide reliable solutions, it is time-consuming and expensive. Besides, scale effects are almost inevitable.

Numerical simulations of the slamming phenomena have become increasingly popular, with the rapid development of computer technology and numerical algorithms. The boundary element method (BEM) based on the potential flow model has achieved many successful developments. For example, Zhao and Faltinsen (1993) studied the water entry of a wedge with various deadrises by a nonlinear BEM. Later, Zhao et al. (1996) extended Zhao and Faltinsen (1993)'s numerical method to general asymmetric bodies. Also, other variations of the BEM have been developed such as Sun and Faltinsen (2009)'s BEM with a flow separation model and Cheng et al. (2018)'s higher-order BEM. However, the BEM has challenges on the viscous flows and the breaking waves, due to the assumption of the inviscid, irrotational fluid (Sun and Wu, 2014).

On the other hand, computational fluid dynamics (CFD) techniques provide an appealing alternative by solving Navier-Stokes (N–S) equations. Many meshfree, moving grid, and Cartesian grid models have been successfully applied to the water impact problems. For example, using the smoothed particles hydrodynamics (SPH) method, Ji et al. (2016) simulated the 2D and three-dimensional (3D) water entry of a wedge, Wang et al. (2019) studied the water entry of an elastomer, and Cheng et al. (2020) modelled the water entry of the 2D bow-flare ship section with different roll angles. By means of the modified moving particle semi-implicit (MPS) method, Sun et al. (2019) analyzed the slamming impacts on the cross deck of the trimaran with rigid and flexible arches. Regarding the moving grid method, Nguyen and Park (2016) combined a curvilinear body-fitted grid-based N–S equation solver with the volume of fluid (VOF) method to simulate water entry of a hemisphere. Xie et al. (2018, 2020) simulated the water entry of a freely falling bow-flared ship section using the commercial software Fluent. Using OpenFOAM, Wang et al. (2021) studied the symmetric and asymmetric water entry of a wedge with the consideration of waves. Also, Hou et al. (2018) investigated the oblique water entry of a cylinder with different inclination angles using the software STAR-CCM+.

Recently, the Cartesian grid methods (Mohaghegh and Udaykumar, 2016; Xie et al., 2020) attract many attentions on the simulation of non-linear free surfaces interacting with complex moving bodies. The immersed boundary (IB) method (Sotiropoulos and Yang, 2014; Yang, 2016) is a well-known Cartesian grid method. In the IB method, the body boundaries are moved in a Lagrangian way on a fixed background (usually Cartesian) grid. The advantages of this method are that the grid generation is much simpler, and no grid reconstruction is needed, compared with the moving grid methods. Therefore, it is much easier to handle complex moving boundaries or the large deformation of free surfaces. In comparison with the meshfree methods, the computational efficiency and numerical stability are improved. Some successful applications on the water impact have been obtained by combining the IB method and the interface capturing method (Li et al., 2019). Kleefsman et al. (2005) studied the water entry of a cylinder and a wedge with prescribed motion by combining a cut cell finite volume method with the VOF method. Similarly, by combining the direct forcing IB method with the level set (LS) method, Zhang et al. (2010) simulated the water entry of a wedge in free motion. Shi et al. (2019) modelled the water impact of a multihull section and a ship section with various roll angles by combining the RBFGCM with the GALS method. Other applications on water impact by the Cartesian grid method can be found in (Bihs and Kamath, 2017; Hu et al., 2018; Zheng et al., 2020).

The aforementioned studies are focused on the water impact of a single body. For the case of the water impact of multiple bodies, Wu (2006) and Yousefnezhad et al. (2014) simulated the symmetric water entry of twin wedges at a constant speed by the BEM. Wu (2006) analyzed the effects of the deadrise angle on the slamming load, the pressure distribution, and the free surface elevation. Yousefnezhad et al. (2014) investigated the effects of the deadrise angle and the gap distance between demi-hulls on the maximum pressure coefficient. However, when it comes to the hydrodynamic interactions between twin wedges, potential flow theory cannot well consider the fluid viscosity and capture the extremely large-amplitude wave (Lu et al., 2011). Shademani and Ghadimi (2017) combined the body-fitted grid method with the VOF method to simulate the water entry of twin wedges at a constant speed. They also investigated the effects of the deadrise angle and the gap width on the impact load and the free surface pattern. In addition, Hu et al. (2017) adopted the CIP (Constrained Interpolation Profile) method and Mahmoodi et al. (2018) used the software ANSYS to simulate the water entry of twin free-falling wedges.

By far, enormous numerical investigations have been conducted on the water impact of a single body, while the attempts on the water impact of twin bodies are much less. Simulation of the water impact of twin bodies is very challenging because the treatment of twin moving bodies is complicated, and violent fluid movement induced by hydrodynamic interference may occur. Moreover, the literatures available lack of analysis on the hydrodynamic characteristics of twin bodies entering water such as local pressures, especially the evolution of the detailed fluid field. Therefore, the motivation of this paper is to study the water impact of twin wedges parametrically and obtain a better understanding of the hydrodynamic interaction mechanism. We analyzed the vertical and horizontal slamming load, the motion response, the impulsive pressure, the pressure distribution, and the fluid field under different drop velocities and gap distances. The present numerical model is based on Shi et al. (2019)'s Cartesian grid multiphase flow model where the RBFGCM and GALS methods are used to treat multiple moving bodies and violent free surfaces, respectively.

Firstly, a case of twin wedges entering water is simulated to validate the accuracy and reliability of the present method. Good convergences of the grid size and the time step are obtained. Then, the water entry of a single wedge under different drop velocities is considered. The effects of the drop velocity on the vertical slamming load, and the impulsive pressure are examined. Afterwards, parametric studies on water entry of twin wedges under various gap distances and drop velocities are performed. In addition, the mechanism of hydrodynamic interaction between two wedges is discussed by examining the variation patterns of the vertical and horizontal slamming loads, the moment, the falling velocity, the impulsive pressure, the pressure distribution, and the fluid field. The present study emphasizes the pressure pattern and the global fluid movement of the wedge at the slamming and transition stages. Some local physical details such as hydroelasticity, turbulence, and air compressibility are not considered in the present study, because they are important only in some special situations such as very small deadrise angles (Lee et al., 2010).

The mathematical model and numerical implementation are given in Section 2. In Section 3, a case of twin wedges entering water is simulated to validate the accuracy of the proposed model, followed by the parametric studies on the water entry of one single and twin wedges. Finally, conclusions and future work are given in Section 4.

2. Mathematical model and numerical solver

2.1. Mathematical model

In this work, an in-house multiphase fluid structure interaction (FSI) model (Shi et al., 2019) on the Cartesian grid is used to simulate the water impact of twin wedges. The governing equations are the incompressible two-phase flow N–S equations including the continuity and

momentum equations, which are expressed as:

$$\nabla \cdot \mathbf{u} = 0 \quad , \quad \text{in} \quad \Omega \tag{1}$$

$$\frac{\partial \mathbf{u}}{\partial t} + \nabla \cdot (\mathbf{u}\mathbf{u}) = -\frac{1}{\rho(\varphi)}\nabla p + \frac{1}{\rho(\varphi)}\nabla \cdot \left[\mu(\varphi)\left(\nabla \mathbf{u} + \nabla \mathbf{u}^{\mathrm{T}}\right)\right] + \mathbf{f}_s, \text{ in}\Omega \tag{2}$$

$$\mathbf{u}|_{\Gamma} = \mathbf{U} \quad and \quad \frac{\partial p}{\partial \mathbf{N}}\bigg|_{\Gamma} = -\mathbf{N}\cdot\frac{d\mathbf{U}}{dt} \tag{3}$$

where $\mathbf{u}$ is the velocity vector. $\mathbf{g}$, ρ, t, p, μ, φ are the gravity vector, the density, the time, the pressure, the dynamic viscosity coefficient and the level set function, respectively. Ω, Γ, and $\mathbf{N}$ represent the whole computational domain, the solid surfaces and the outward normal vector of the solid surface, respectively. $\mathbf{U}$ is the velocity vector of the solid body. $\mathbf{f}_s$ is used to consider the effects of the surface tension with $\mathbf{f}_s = \sigma\kappa\delta(\varphi)/\rho(\varphi)$, where σ is the surface tension coefficient, κ is the interface curvature, $\mathbf{n}$ is the normal vector of the fluid-gas interface, and δ is the discrete delta function.

The GALS equations are adopted to describe the free surface motion, where the level set function and its gradient vector are solved in a fully coupled way to improve the accuracy of the interface representation. The GALS equations (Nave et al., 2010) are expressed as:

$$\frac{\partial \varphi}{\partial t} + \mathbf{u}\cdot\nabla\psi = 0 \tag{4}$$

$$\frac{\partial \psi}{\partial t} + \mathbf{u}\cdot\nabla\psi = -\nabla\mathbf{u}\cdot\psi \tag{5}$$

where ψ is the gradient vector with $\psi = \nabla\varphi$. $\nabla\psi$ and $\nabla\mathbf{u}$ are the gradient and velocity deformation matrices, respectively. The discontinuous water-air interface is treated by the smoothed Heaviside function in a diffused way.

2.2. Numerical solution of N–S equations

A time semi-implicit finite difference method is used to solve the N–S equations on a staggered Cartesian grid. The convective term is discretized by a higher-order total variation diminishing monotonic upstream-centered scheme for conservation laws (TVD-MUSCL) (Leer, 1997) with explicit treatment in time. The diffusive term is handled by the second-order central difference scheme with the semi-implicit treatment in time. The N–S equations are integrated in time by the fractional step method (Kim and Moin, 1985), combined with the TVD second-order Runge-Kutta (TVD-RK2) scheme. The RBFGCM is employed to enforce the velocity Dirichlet and the pressure Neumann boundary conditions in Eq. (3), and thus to represent the existence of the moving bodies. In addition, a preconditioned bi-conjugate gradient stabilize (BICGSTAB) method (Van der Vorst, 2003) with a diagonal storage format is used to solve the large sparse positive definite matrix, which comes from the discretization of Poisson equations for pressure.

2.3. Treatment of the solid boundaries by the RBFGCM

Accurate representation of the moving boundaries is a challenge for the IB method because the immersed boundaries are not imbedded in the computational grid. To enforce the boundary conditions on the moving bodies, the RBFGCM (Xin et al., 2018) is adopted in the present study. The key step of this study is to track the arbitrary immersed boundaries implicitly, by fitting an iso-surface function with the radial basis function. The ghost cells can be identified directly by using the signed distance property of the iso-surface function, to represent the position of the moving boundaries. As shown in Fig. 1, the ghost cells (GC) are identified as the cells inside the solid bodies and adjacent to the fluid cells, the solid cells (SC) are the cells inside the solid bodies and do not belong to the ghost cells, and the fluid cells are the cells inside the
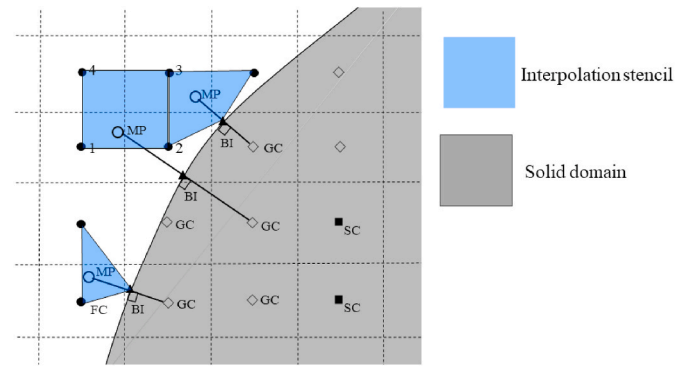

Fig. 1. Bilinear interpolation stencils for three situations.

fluid domain. To perform interpolation reconstruction, the mirroring point (MP) is introduced by mirroring the ghost cell to the outside of the body surface. The boundary point (BI) at the body surface is in the middle between the ghost cell (GC) node and the mirroring point (MP). The fluid variables (pressure or velocity component) of the mirroring points are reconstructed by a bilinear interpolation scheme, as the interpolation stencils are presented in Fig. 1. The fluid variables of the ghost cells are determined by mapping from values of the mirroring points in the fluid domain. No-slip boundary conditions are imposed implicitly on the moving boundaries, when the N–S equations are solved on the whole computational domain by a standard finite difference scheme. The benefits are that the treatment for the complex moving bodies is simplified because the numerical discretization is relatively independent of the geometrical complexity of the immersed bodies.

2.4. Treatment of the free surface by the GALS method

The GALS equations can be re-expressed in the characteristic forms:

$$\frac{d\varphi}{dt} = 0 \text{ and } \frac{d\psi}{dt} = -\nabla\mathbf{u}\cdot\psi \tag{6}$$

Consequently, the ordinary differential equations are obtained. The GALS equations in Eq. (6) are solved in two steps. Firstly, the Shu-Osher RK3 scheme is adopted to solve the characteristic curve equation $\partial x(\tau)/\partial\tau = \mathbf{u}(\mathbf{x}(\tau),\tau)$ by backward integration to determine $\mathbf{x}_C$, where $\mathbf{x}_C$ is a characteristic displacement inside the cell. The LS function and the gradient vector at the point $\mathbf{x}_C$ are interpolated by the high-order Hermite cubic polynomial scheme. Secondly, the LS function and its gradient vector are updated by solving Eq. (6). The value of the LS function $\varphi(\mathbf{x}_C)$ at the point $\mathbf{x}_C$ is that of the LS function at the new time step since the LS function is constant along the characteristic curve. The gradient equation is solved by an explicit trapezoidal scheme forward integration along the characteristic curve. In addition, a Lagrange polynomial interpolation scheme is used to interpolate the velocity vector at arbitrary positions. The detailed numerical implementation can be referred to Shi et al. (2019).

2.5. Numerical validation

The present numerical model has been demonstrated extensively by many cases such as flows around one and two oscillating cylinders (Xin et al., 2018), nonlinear sloshing, and the water entry of a complex moving body (Shi et al., 2019). The fluid load, the local pressure, and the free surface elevation agree well with the experimental, analytical, and numerical results. Further, the water entry of twin wedges is simulated to verify the accuracy of the proposed model for water impact of two moving bodies. The total mass of the wedge is 13.522 kg. The breadth B of the wedge is 0.2 m and the deadrise angel is $\alpha = 45^{\circ}$. The initial velocity V_o is set to be 0.95623 m/s when the wedge touches the water surface. The computational domain is [0 m, 2.4 m] × [0 m, 1.6 m] with a

water depth of 1.0 m, as the geometric model is shown in Fig. 2. The wedge surface is represented by 120 Lagrangian points with the minimum grid size of $\Delta s = 0.004$ m. The twin wedges are symmetrically arranged with a horizontal distance of $G = B$. The densities of water and air are 1000 kg/m^3 and 1 kg/m^3, respectively. The dynamic viscosity coefficients of water and air are 1.1×10^{-3} kg/m/s and 1.7×10^{-5} kg/m/s, respectively. The acceleration of the gravity is $|\mathbf{g}| = 9.81$ m/s^2. The velocity no-slip ($\mathbf{u}|_\Gamma = \mathbf{U}$) and the pressure Neumann boundary conditions ($\partial p/\partial \mathbf{N}|_\Gamma = 0$) are enforced on the wedge surface by the present RBFGCM (Xin et al., 2018). On the top boundary, the velocity slip boundary condition ($\partial \mathbf{u}/\partial \mathbf{N} = 0$) is applied and zero pressure is set as the reference of the atmospheric pressure. On the bottom and side boundaries, the velocity slip ($\partial \mathbf{u}/\partial \mathbf{N} = 0$) and pressure Neumann ($\partial p/\partial \mathbf{N} = 0$) boundary conditions are enforced.

To validate the reliability of the present multiphase flow model, convergence tests on the grid size and the time step are conducted. Three non-uniform grids are used to examine the grid convergence. The detailed grid information is given in Table 1 $\Delta x_{\max}$ and $\Delta x_{\min}$ are the maximum and minimum grid sizes in the x-direction, respectively. $\Delta y_{\max}$ and $\Delta y_{\min}$ are the maximum and minimum grid sizes in the y-direction, respectively. The refined uniform grid is applied on the local domain of [0.7 m, 1.7 m] × [0.75 m, 1.15 m]. Fig. 3 shows the time history of the vertical loads and velocities for the present method on three grids. Hu et al. (2017)'s numerical results by the CIP method are also provided as a reference. The time step is restricted by the CFL (Courant-Friedreichs-Lewy) condition. The time-relaxation coefficients are chosen as $\omega_{CFL} = 0.4$. The present vertical load is obtained by integrating the surface pressure and then subtracting the gravity. The present vertical loads and velocities by the current model on three grids agree reasonably with Hu et al. (2017)'s numerical results, which confirms the accuracy of the present method. Also, the hydrodynamic load becomes smoother as the grid is refined. The vertical loads and the velocities on three grids are very close to each other, though slight deviations on the vertical velocity between the fine grid and the medium grid are observed. The deviations may be caused by the large grid ratio between the Lagrangian grid on the wedge surface and the Eulerian grid on the computational domain. When the grid convergence test is conducted with more Lagrangian points of 200, a better convergence performance can be obtained. However, to achieve a balance between the solution quality and computational cost, the medium grid of $y_{\min} = 0.002$ m and 120 Lagrangian points are adopted in the following computations.

To investigate the time independence, three time-relaxation coefficients are chosen as $\omega_{CFL} = 0.8$, 0.4, and 0.2. The corresponding time step is about 3.2×10^{-4} s, 1.6×10^{-4} s, and 0.8×10^{-4} s, accordingly. Fig. 4 shows the time history of the vertical loads and velocities on three time-relaxation coefficients obtained by the present method and from Hu et al. (2017)'s CIP method. Again, good agreements are achieved between the present results and Hu et al. (2017)'s simulations. The forces and velocities on three time-relaxation coefficients are almost indistinguishable, indicating that the time convergence is achieved. Note that small amplitude oscillations occur on the vertical loads with
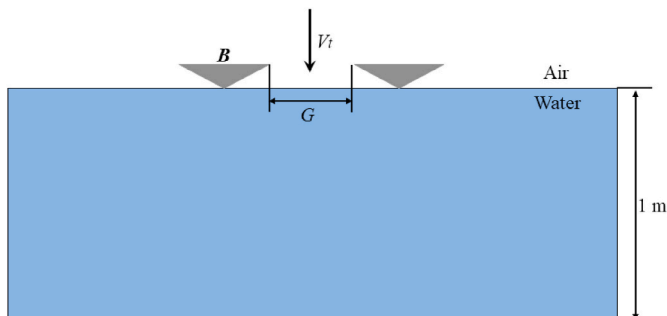
Table 1
Convergence tests on three non-uniform grid systems.

	Grid number	$\Delta x_{\min}$	$\Delta x_{\max}$	$\Delta y_{\min}$	$\Delta y_{\max}$
Coarse grid	388 × 323	0.008	0.08	0.004	0.04
Medium grid	678 × 527	0.004	0.04	0.002	0.02
Fine grid	1017 × 884	0.002	0.02	0.001	0.01

the present model. These force oscillations are often encountered in the sharp interface IB method (Lee et al., 2011; Liu et al., 2014). They are caused by the local mass non-conservation around the moving boundary and can be reduced by refining the grid or introducing interface treatment strategies.

The present pressure distribution over the left wedge is compared with the Wu (2006)'s similar solution in Fig. 5. The dimensionless coefficients C_p and x^* are defined as $C_p = Pr/\rho_w V^2$ and $x^* = x/BVt$, where ρ_w, V, and x are the density of the water, the instantaneous velocity, and the horizontal distance away from the keel of the wedge, respectively. The pressure profile predicted by the present method reasonably agrees with Wu (2006)'s similar solution, except that the peak pressure around the keel of the wedge is slightly overestimated. The deviations are acceptable, because the free motion, the fluid viscosity, and the gravity are considered in the present numerical model, but not in Wu (2006)'s similar solution. The profile of the pressure distribution is unsymmetric when another wedge is nearby. The pressure crest of bevel edge close to another wedge is much larger than that away from another wedge.

Fig. 6 shows the free surface profiles around the two wedges at three moments with the medium grid and $\omega_{CFL} = 0.4$. The free surface profile at $t = 0.065$ s is consistent with that at $t = 0.0678$ s by Hu (2017)'s CIP method. When the wedge initially hits the free surface, the free surface is pushed away along two sides of the wedge at $t = 0.03$ s. As the wedge continues to pierce through the free surface, the wetted area increases. Two symmetric jet flows are fully attached to each wedge surface begin to detach from the knuckles. At $t = 0.065$ s, the jet flows move away from the knuckles and begin to curl slightly inward under the effects of the gravity, yielding an open cavity at the gap between two wedges. Afterwards, the jet becomes thinner. The two jet roots at the gap move toward each other, and thus the open cavity becomes a closed one at $t = 0.09$ s. Also, the jets begin to merge together and form an upward jet flow. The evolution process of the free surface is similar to the results presented by Mahmoodi et al. (2018).

3. Results and discussion

In this section, the water entry of one and two free-falling wedges is parametrically investigated. Again, the accuracy of the present model is confirmed by comparing the present results of single wedge entering water with the experimental data. Also, the results of single wedge entering water provide an effective reference for the investigation of twin wedges entering water. In the cases of twin wedges entering water, the fluid load, the moment, the impulsive pressure, the pressure distribution, and the fluid field are analyzed. Further, the interaction mechanism between the two wedges is discussed.

3.1. Water entry of a free-falling wedge

Following Aarsnes (1996)' experimental work and Sun (2007)'s BEM, the considered wedge has a triangle profile with a breadth of $B = 0.3$ m, and the deadrise angle is $\alpha = 30°$. The total length of the wedge section is 1 m, and the length of the measuring section is 0.1 m. The total weight of the drop rig is 288 kg. In the present simulation, the computational domain is set as [0 m, 2 m] × [0 m, 1.6 m], and the water depth is 1 m. The keel of the wedge is set right above the initial water surface at (1 m, 1 m). As shown in Fig. 7, five pressure sensors named from P1 to P5 are placed on the right side of the wedge with a distance from the keel of the wedge 0.03 m, 0.06 m, 0.09 m, 0.12 m, and 0.15 m, respectively.

Fig. 2. Geometric model of the twin wedges.
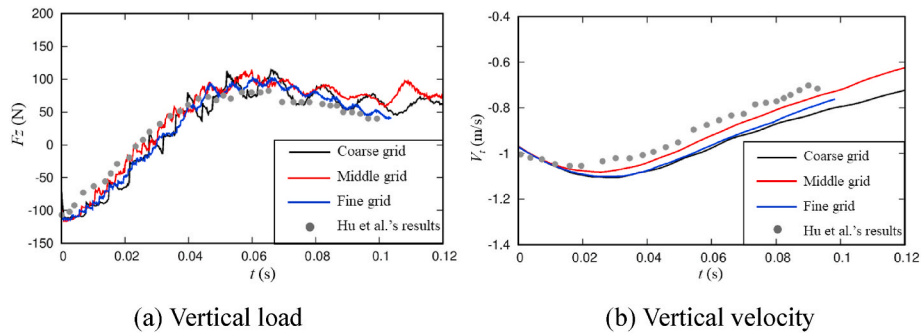
(a) Vertical load

(b) Vertical velocity

Fig. 3. Vertical loads and velocities versus time with different grid sizes and compared with Hu et al. (2017)'s results.

(a) Vertical load
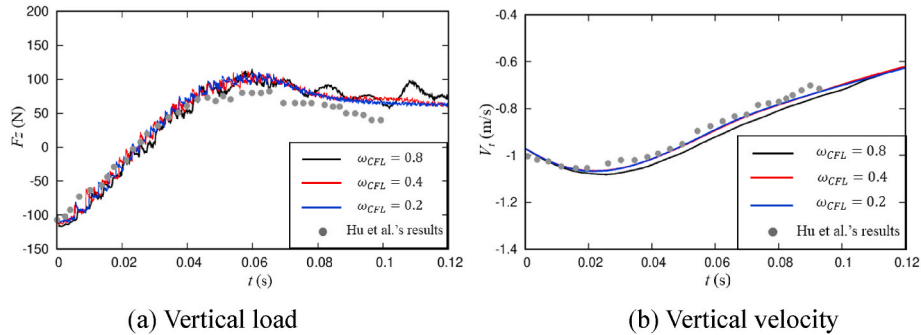

(b) Vertical velocity

Fig. 4. Vertical loads and velocities versus time with different time-relaxation coefficients and compared with Hu et al. (2017)'s results.
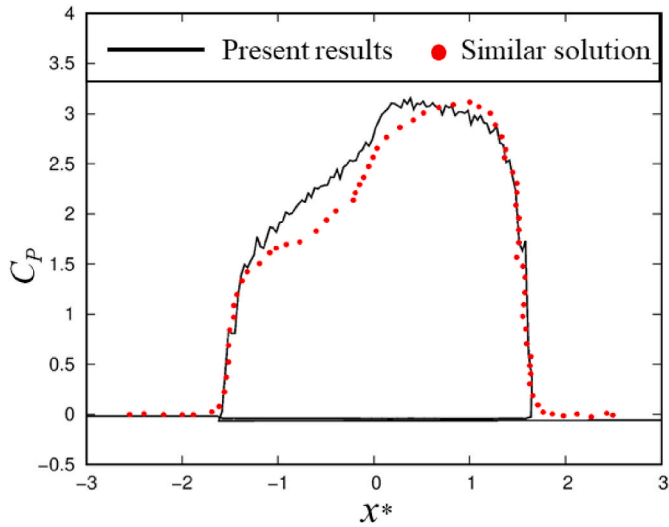

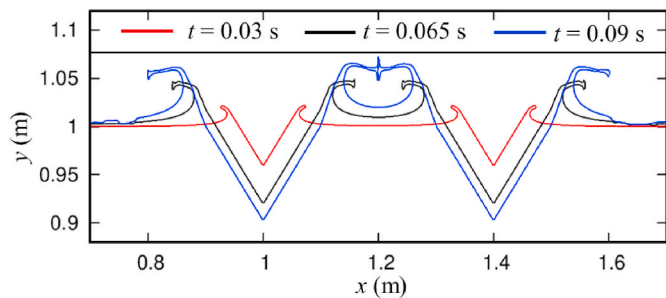**Fig. 5.** Pressure distribution around the left wedge obtained by two methods.

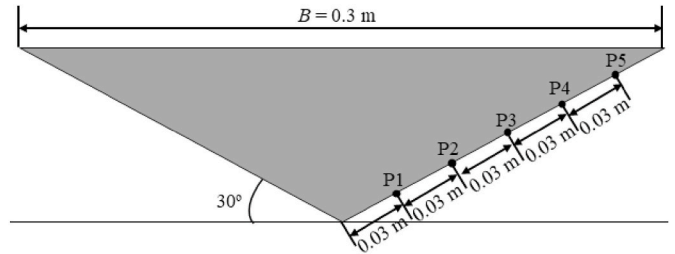**Fig. 6.** Free surface profiles around the twin wedges at three moments.

Fig. 7. The dimensions of the wedge and the arrangement of the pressure gauges.

Four drop velocities are chosen as $V_0 = 1.55$ m/s, 1.91 m/s, 2.42 m/s and 3.05 m/s to investigate the effects of the drop velocity.

According to the convergence studies in Section 2.5, the medium grid of $y_{min} = 0.002$ m and the time coefficient of $\omega_{CFL} = 0.4$ are used. Fig. 8 shows the time evolution of the vertical slamming force for the four velocity cases. The dotted lines separate the variation of the slamming force into two stages. The slamming forces predicted by the current model are in overall agreement with Aarsnes (1996)' experimental data and the results of Sun (2007)'s BEM for four drop velocities. Specifically, the present peak slamming forces are closer to those of Sun (2007)'s BEM and slightly larger than Aarsnes (1996)' experimental data. The possible reason is the 3D effects. Zhao et al. (1996) mentioned in their free drop experiment that 3D effects suppressed the maximum vertical impact load about 20%. It should be noted that some oscillations are shown in the experimental data, due to the vibration of the falling trolley. In addition, the occurrence moments of the present peak loads are close to those in the experimental data for $V_0 = 1.55$ m/s, 1.91 m/s, and 3.05 m/s, while they lag slightly behind those in Sun (2007)' BEM for four drop velocities. One possible reason is that the air effects are considered in the present multiphase flow model but not in Sun (2007)'s BEM. The air between the free surface and the wedge buffers the free surface against touching the wedge surface. This yields that the peak
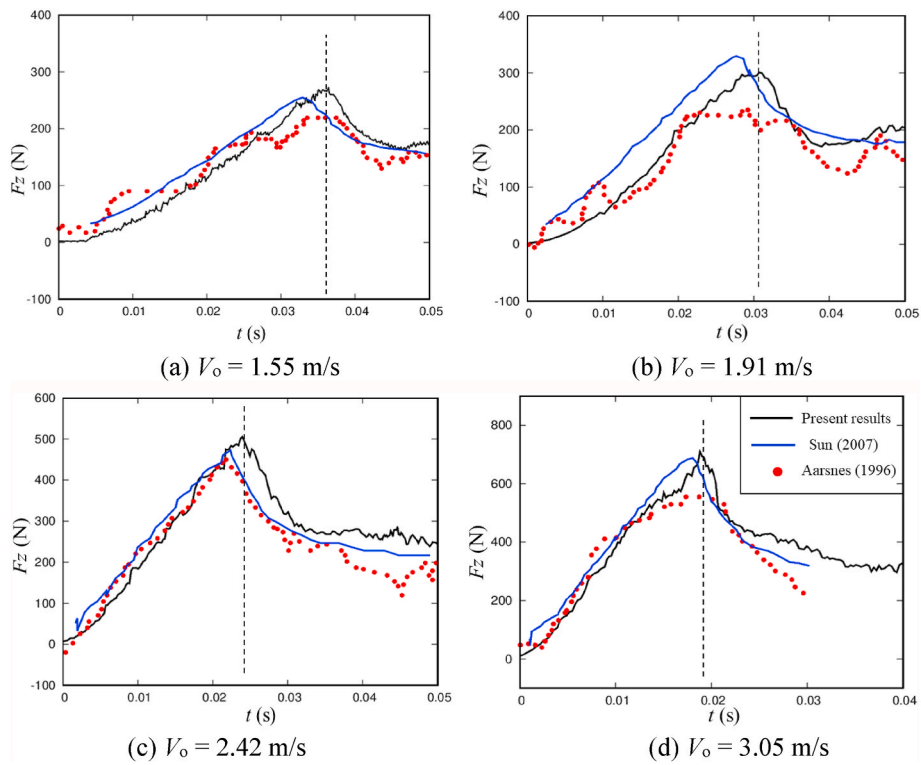
Fig. 8. Time history of the vertical slamming load for four drop velocities.

load is reduced, and its occurrence moment is delayed. Another reason may be that the water-air interface is treated in a diffused way by the smoothed Heaviside function for its simplicity and robustness. Consequently, the pressure is smoothed over several grids, which delays the occurrence moment of the maximum slamming load. Fortunately, the lag phenomena caused by the smoothed function can be relieved by refining the grid size or decreasing the time step.

As shown in Fig. 8, the force variations are divided into the slamming and transition stages. Following Wang et al. (2015)'s definition, the slamming stage starts when the wedge touches the water surface and ends when the main flow reaches the knuckles of the wedge. Then, the transition stage begins, and it ends when the top side of the wedge is below the still water level. The dividing line between the slamming and transition stages is the dotted line, as shown in Fig. 8. At the slamming stage, the slamming loads increase rapidly from zero to the maximum when the knuckles of the wedge hit the main flow. The added mass of the wedge rises quadratically with the wetted breadth as the wedge penetrates the water. The peak load rises from 250 N to 700 N when the drop velocity increases from 1.55 m/s to 3.05 m/s. In addition, the peak load occurs sooner with the rising of the drop velocity, because the wedge is
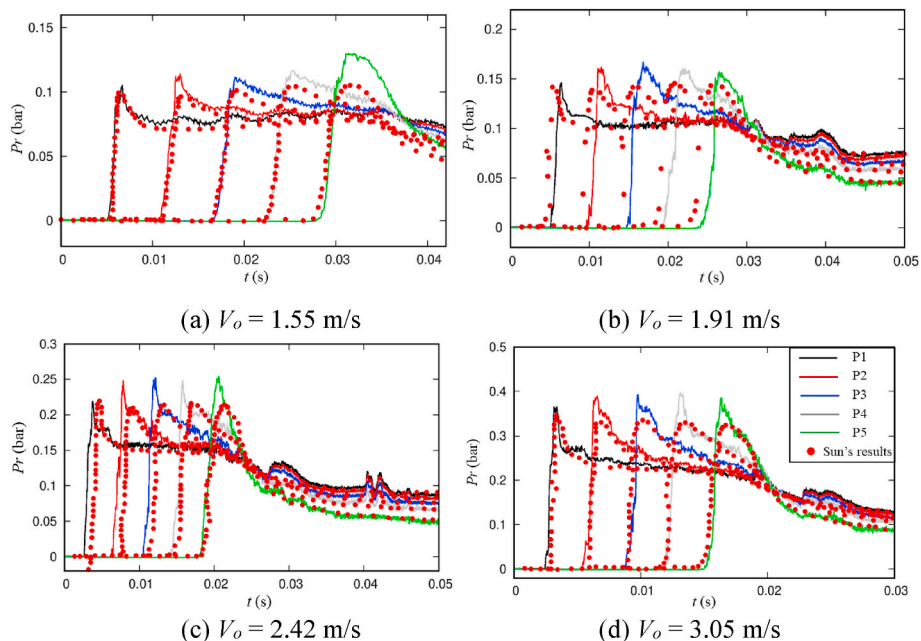

Fig. 9. Local pressures from P1 to P5 on the wedge surface for four velocities.

wetted faster. At the transition stage, the slamming load decreases to a plateau value quickly when an equilibrium is reached between the fluid force and the gravity. However, the dropping speed at the transition stage is smaller than the growing speed at the slamming stage. At this moment, the free surfaces are separated from the knuckles of the wedge. The rate of change of the added mass reduces, leading to a dramatic drop in the slamming load (Wang et al., 2015). In addition, the equilibrium load at the transition stage rises from about 150 N for $V_o = 1.55$ m/s to approximately 320 N for $V_o = 3.05$ m/s. In general, the maximum impulsive load increases remarkably and the persisting time of the slamming load is shortened with the rising of the drop velocity.

The time histories of the impact pressures on the five measuring points P1–P5 under four velocities are presented in Fig. 9. The variation trends of the pressure agree with Sun's BEM satisfactorily. The sharp peak pressures are well captured in the present study, while the peak pressures by Sun's BEM are much smooth. The peak pressures calculated by the present method are overpredicted slightly, compared with Sun's BEM. Considering the complexity of the physical phenomena, the discrepancies are within the tolerance.

The peak pressures at five measuring points appear successively from the keel to the knuckle. The impact pressure grows to the maximum instantaneously when the spray root of the free surface touches the measuring point. Afterwards, the measuring point is immersed into the water gradually. The impact pressure decreases quickly, followed by a plateau phase, because the variation rate of the added mass decreases dramatically. Different positions of the wedge experience similar peak pressures since the velocity of the wedge changes little during the water entry. As the drop velocity increases, the maximum impact pressure grows significantly, and the peak pressure occurs earlier because the wedge gets wetted in a faster speed. Moreover, the larger the impact velocity is, the more significant the nonlinearity and instantaneity is. According to the flat plate approximation (Faltinsen et al., 2005), the slamming pressure is proportional to the impact velocity. A larger slamming pressure occurs in a shorter time when the wedge enters the water in a larger velocity. Therefore, the crest of the pressure curve is sharper. In addition, to capture the sharp slamming pressure in high-speed water entry, the high-resolution grids and small-time steps are demanded.

Further, the pressure distributions on the wedge surface predicted by the present model are compared with Wu (2006)'s similar solutions for $V_o = 1.91$ m/s and $V_o = 3.05$ m/s in Fig. 10. The dimensionless coefficients C_p and x^* are defined in Section 2.5. As expected, symmetric pressure distributions are observed with respect to the centerline for two drop velocities. The present pressure distributions generally agree with Wu (2006)'s similar solution for both velocities, though the present maximum pressure coefficients are slightly overpredicted. In addition, Fig. 11 shows the pressure distributions on the wedge surface at five
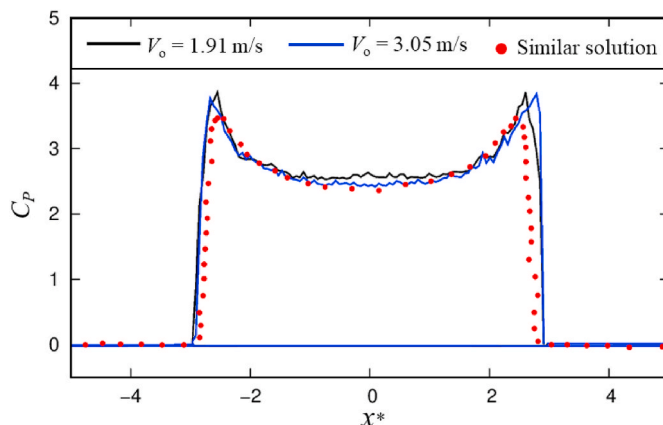
instances for $V_o = 1.91$ m/s and $V_o = 3.05$ m/s. At $t = 0.005$ s, the pressures are distributed at a narrow area of the wedge. The minimum pressure appears around the keel of the wedge and the maximum pressure occurs at the intersection points between the spray roots and the wedge surface. The pressure profile gets gradually widened with the time advancement because the wetted area of the wedge gets larger. On the other hand, the peak of the pressure profile first increases and then declines. The turning moment for $V_o = 1.91$ m/s is about $t = 0.02$ s and it is $t = 0.01$ s for $V_o = 3.05$ m/s. According to the flat plate theory (Faltinsen, 2005), the pressure on the body can be divided into the slamming pressure related to the falling velocity and the added-mass pressure related to the acceleration. The added mass pressure is much smaller than the maximum slamming pressure. At $t = 0.01$ s, the velocity reaches the maximum, leading to a large slamming pressure. Then, the velocity decreases, and thus the slamming pressure decreases.

3.2. Water entry of twin free-falling wedges

In this section, the water entry of twin free-falling wedges is studied. The effects of the gap distance and the drop velocity on the slamming load, the pressure distribution, and the fluid field are investigated. The gap coefficient is defined with $G^* = G/B$, where G is the gap distance between the apexes of two wedges. The side boundaries of the computational domain are varied with the gap distance. The keel of the left wedge is 1 m away from the left boundary, and the keel of the right wedge is 1 m away from the right boundary. Similar to Section 3.1, a nonuniform grid is applied with the minimum grid size of $y_{min} = 0.002$ m in the refined domain around the wedges. The time-relaxation coefficient is set as $\omega_{CFL} = 0.4$. Other physical and computational parameters keep the same with Section 3.1, and the same four drop velocities are chosen as $V_o = 1.55$ m/s, 1.91 m/s, 2.42 m/s, and 3.05 m/s. To investigate the effects of the gap distance, four gap coefficients are chosen as $G^* = 0.2$, 0.5, 1, and 3. Note that the single wedge case is equivalent to the water entry of twin wedges at an infinite distance.

Firstly, the effects of the gap distance on the slamming load and moment are investigated. Fig. 12 shows the comparison of the time evolution of the vertical slamming force (Fz) on the left wedge at four gap distances for four drop velocities. The time evolution of the horizontal force (Fx) and the moment (Me) are presented in Figs. 13 and 14. The moment arm is calculated with respect to the keel of each wedge. The slamming forces of the single wedge entering water are presented for reference. The results on the right wedge are not presented because the right wedge is symmetric with the left one. At the initial slamming stage, the vertical slamming forces are almost overlapped. The horizontal forces and the moments are approximately zero at all gap distances. The results indicate that the hydrodynamic interaction between two wedges for various gaps are negligible at the initial slamming stage.

As the wedge moves into the water, obvious discrepancies on the fluid forces and moments start to appear for a small gap distance, which implies the significant hydrodynamic interaction. The vertical slamming loads increase first and decrease then for all gap distances. As the gap narrows at $G^* \geq 0.5$, the maximum vertical and horizontal loads as well as the moments grow slightly, while sharp increases are observed at $G^* = 0.2$. The peak values of the peak loads and moments occur nearly at the same time. The occurrence moments of the peak loads and moments seem to be independent of the gap distances, while they occur earlier for a larger drop velocity, as observed from the dotted lines in Figs. 12–14. However, the patterns of the slamming loads and the moments are hardly affected by the water entry velocity. It should be noted that the horizontal fluid forces are negative because the water at the gap pushes the two wedges away from each other. The horizontal fluid forces are smaller about one order of magnitude than the corresponding vertical forces for all gap distances and drop velocities, due to the vertical water entry. In addition, as the drop velocity increases, the peak vertical and horizontal loads as well as the peak moments at all gap distances grow.

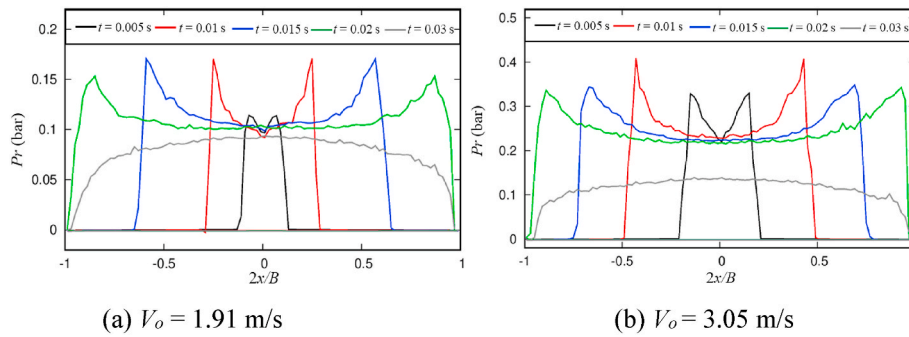When twin wedges are far away from each other such as $G^* = 3$, the

Fig. 10. Comparison of pressure distributions for two drop velocities.

Fig. 11. Pressure distributions on the wedge surface at five instants for two drop velocities.
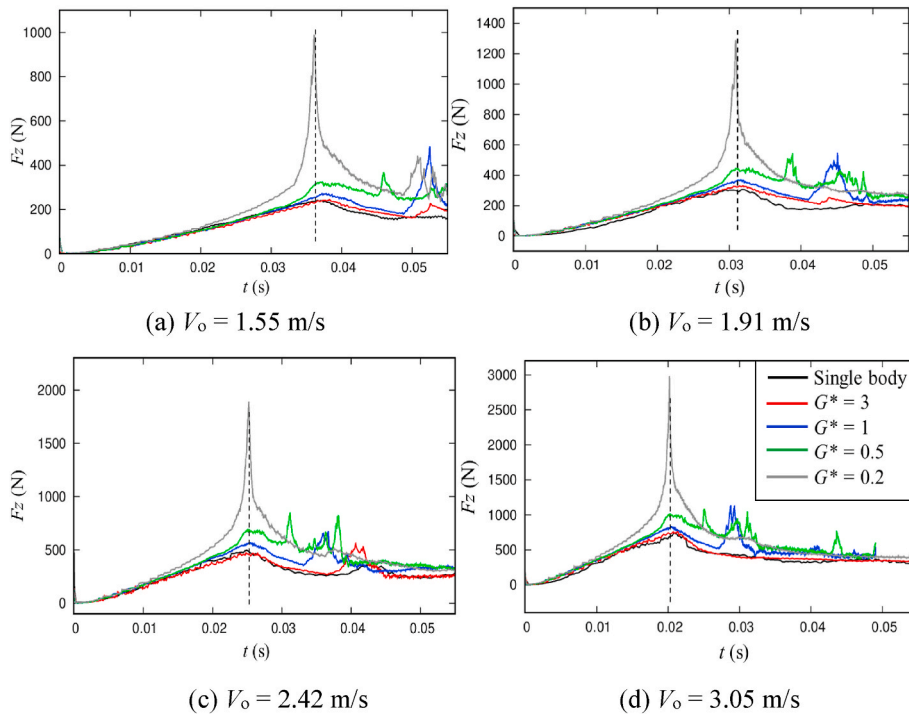

Fig. 12. Time history of the vertical loads on the left wedge for four drop velocities.

curves of the vertical slamming loads are almost coincident with those of a single wedge entering water for four drop velocities. The horizontal slamming loads and the moments are almost zero. When the gap distance is $G^* = 1$, there is no apparent change in the peak vertical load, while a second smaller peak load occurs at the transition stage. On the other hand, the horizontal loads and the moments grow slowly at the transition stage. As the gap distance narrows to $G^* = 0.5$, significant hydrodynamic interaction occurs. The maximum vertical loads are approximately 30% larger than those in the single wedge case for four drop velocities. Several successive peak loads appear at the transition stage. Also, a single-peak pattern is observed in the horizontal fluid forces and the moments. When twin wedges are in closest positions $G^* = 0.2$, the maximum vertical load increases sharply, which is over four times as large as that of the single wedge case. Moreover, the peak horizontal force and moment rise sharply, much larger than those at $G^* = 0.5$. The hydrodynamic effects of the two wedges are similar with a complex single body. The clearly-observed different hydrodynamic characteristics will be explained later in this section. It can be seen that the slamming loads and the moments are remarkably affected by the gap distance when the two wedges are in a small distance ($G^* < 1$).

Fig. 15 shows the time history of the dimensionless velocity at four gap distances for four drop velocities. The dimensionless velocity is

defined by the Froude number (*Fr*) with $Fr = V_t / \sqrt{|\mathbf{g}|H}$, where V_t is the water entry velocity and H is the water depth. The results of the single wedge entering water are presented for the reference. At the initial slamming stage, the velocities at all gap distances keep almost coincident and increase rapidly for four drop velocities. Then, velocity curves at all gap distances branch in different directions, because the effects of the hydrodynamic interaction are more significant for a smaller gap distance. The branching moment occurs earlier from $t = 0.03$ s to $t = 0.01$ s for a smaller gap distance and a larger drop velocity, which is in consistent with the occurrence moment of the peak load. The falling velocities for $V_0 = 1.51$ m/s and 1.91 m/s at two larger distances $G^* = 1$ and $G^* = 3$ keep an increase trend, but rising speed is smaller at the transition stage. The velocities for $G^* = 0.2$ and $G^* = 0.5$ increase first, and then continuously decrease. It is caused by the fact that the vertical loads for $G^* = 0.2$ and $G^* = 0.5$ are larger than the gravity of the wedge at the later stage.

For water impact, the extremely large impulsive pressures at local positions can lead to structural damage, posing serious challenges to the structural design of marine structures. Figs. 16 and 17 show the time evolution of the local pressures at five positions P1 to P5 on the left wedge at four gap distances for $V_0 = 1.91$ m/s and 3.05 m/s,
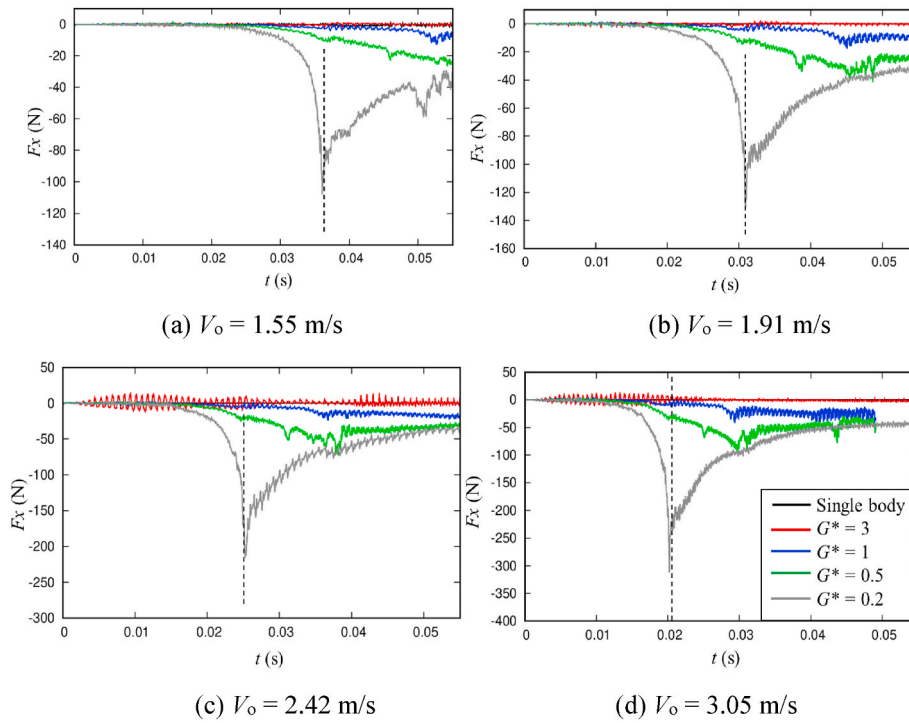
Fig. 13. Time history of the horizontal loads on the left wedge for four drop velocities.
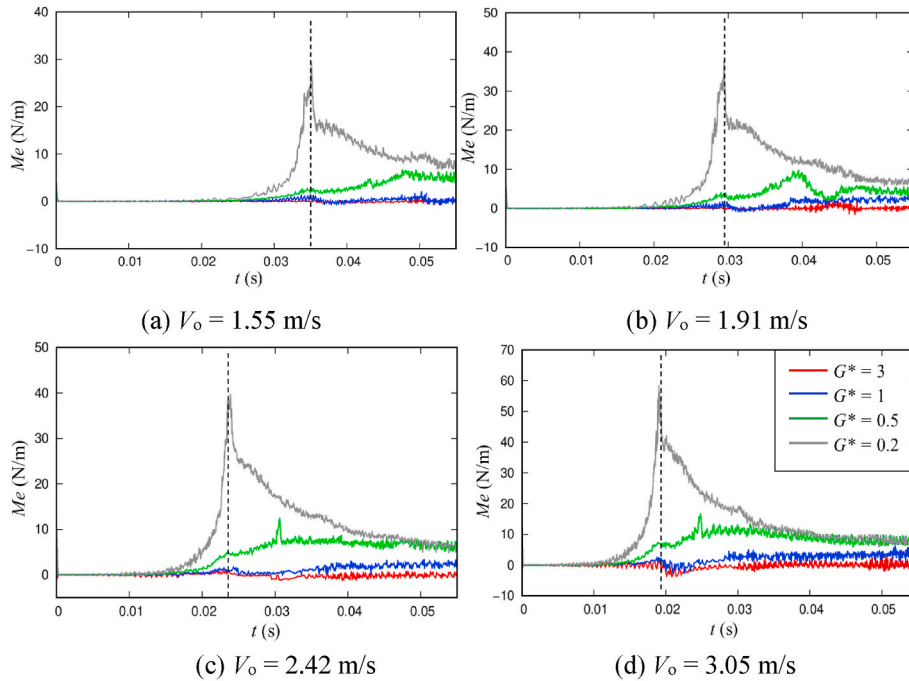

Fig. 14. Time history of the moments on the left wedge for four drop velocities.

respectively. It can be seen that the peak pressures at P1 to P5 keep almost the same as the gap distance narrows at the slamming stage, while they are nearly doubled when the drop velocity increases from 1.91 m/s to 3.05 m/s. On the other hand, the pressure characteristics at the transition stage are quite distinct for different gap distances, while they are hardly affected by the drop velocity. As the wedge further moves into the water, the pressure at four gap distances decreases to a similarly low level. At this moment, the slamming pressure induced by the hydrodynamic interaction reduces and the hydrostatic pressure

plays an important role.

For $G^* = 3$ in Figs. 16(a) and 17(a), the variation trends of the pressures at five points are similar with those in the single wedge case. When the gap narrows to $G^* = 1$ in Figs. 16(b) and 17(b), the entire wedge experiences an obvious pressure pulse at the transition stage, which is consistent with the second peak load in Fig. 12. The values of the pulse pressures at P1 and P2 are larger approximately 50% than those at the slamming stage. When the gap continues to narrow such as $G^* = 0.5$, the pressure changes drastically due to the violent
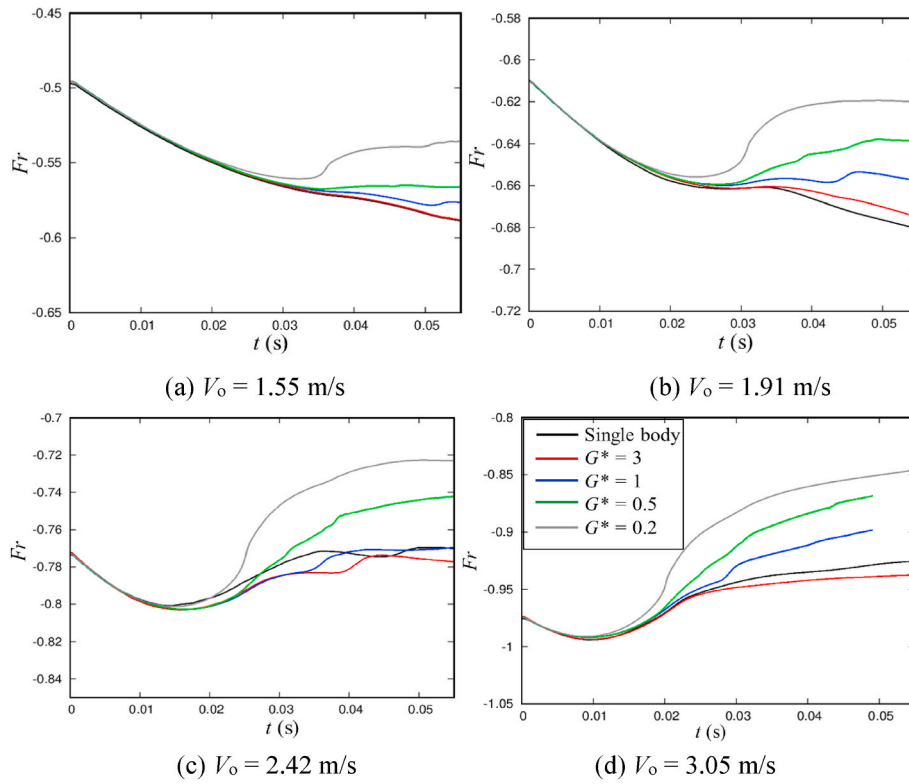
(a) V_o = 1.55 m/s

(b) V_o = 1.91 m/s

(c) V_o = 2.42 m/s

(d) V_o = 3.05 m/s

Fig. 15. Time history of the falling velocity on the left wedge for four drop velocities.

(a) G^* = 3

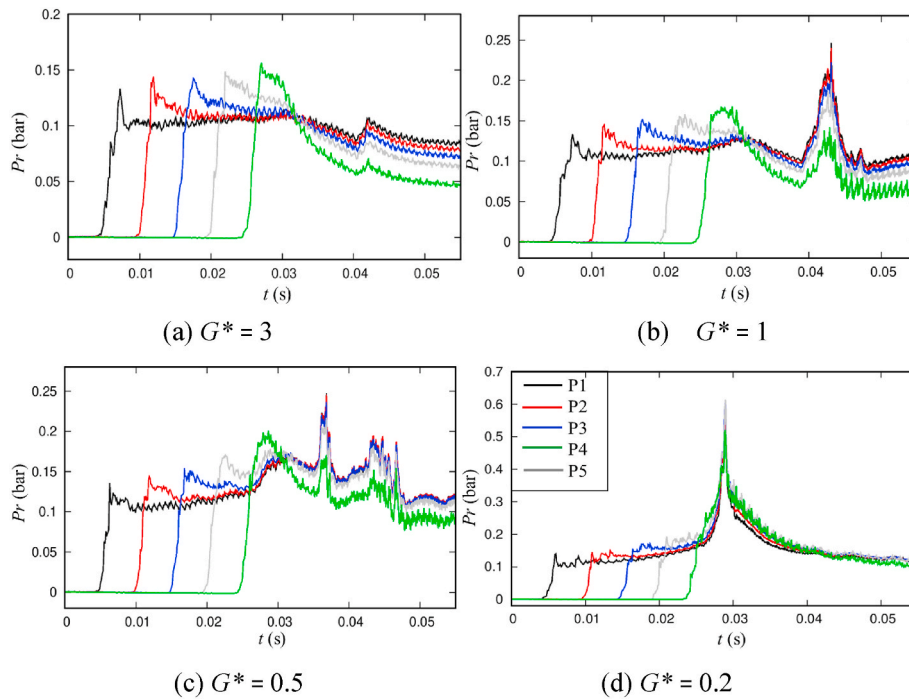(b) G^* = 1

(c) G^* = 0.5

(d) G^* = 0.2

Fig. 16. Local pressures at five positions P1 to P5 on the left wedge for V_o = 1.91 m/s at four gap distances.

hydrodynamic interaction. Several small pressure pulses are observed in Figs. 16(c) and 17(c). When the gap narrows to the minimum of $G^* = 0.2$, the dramatic pressure pulse occurs at the transition stage in Figs. 16 (d) and 17(d), which corresponds to the extremely large peak load in Fig. 12. The values of the pressure pulses at P1 to P5 are close to each other, and they are approximately three times larger than the peak

pressures at the slamming stage. It can be observed that the maximum pressure and the pressure pulse occur earlier for a larger drop velocity. Also, the pressures especially near the keel of the wedge are significantly affected by hydrodynamic interaction between two wedges for $G^* \leq 1$. The huge pressure pulse may be caused by the cavity formed in a small gap distance, which will be explained later. The cavity closure can result
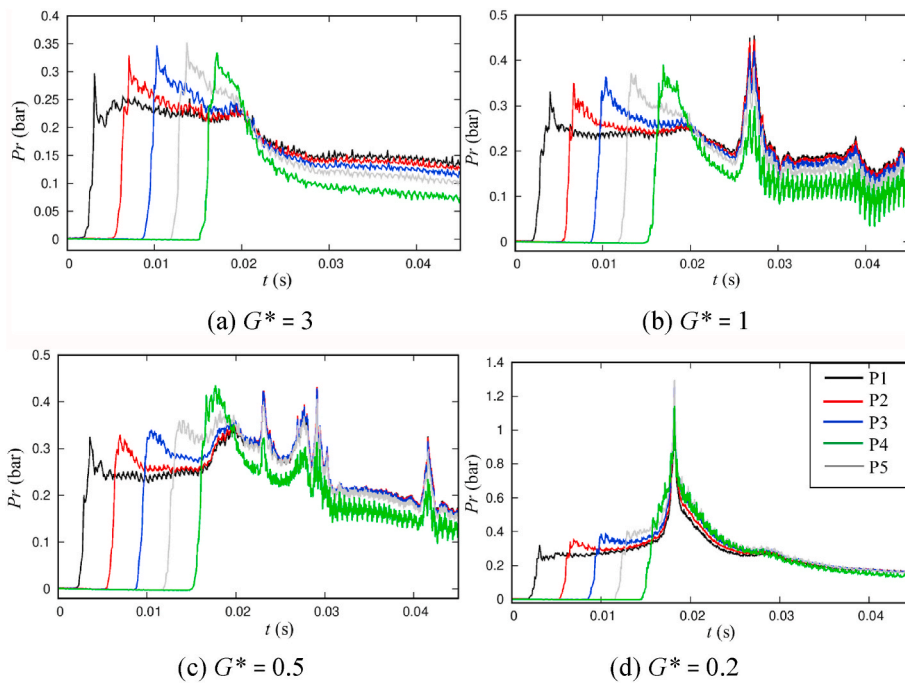
Fig. 17. Local pressures at five positions P1 to P5 on the left wedge for $V_o = 3.05$ m/s at four gap distances.

in the pressure oscillations. As shown in Fig. 16(b and c), Fig. 17(b and c), obvious pressure oscillations are observed after the pressure pulse, especially for a higher drop velocity.

Fig. 18 presents the pressure distributions on the left wedge at four gap distances at four instants for $V_o = 3.05$ m/s. The water entry process is characterized by four major phases including that the wedge touches the water initially, is partially wetted, is fully wetted, and is immersed into the water. As is shown in Fig. 18, the wedge experiences approximately symmetric pressure distributions at two moments $t = 0.005$ s and $t = 0.01$ s for four gap distances, which indicates the negligible hydrodynamic interaction. For $G* = 3$, minor asymmetric pressure is observed at $t = 0.02$ s. As the wedge is immersed into the water at $t = 0.04$ s, the
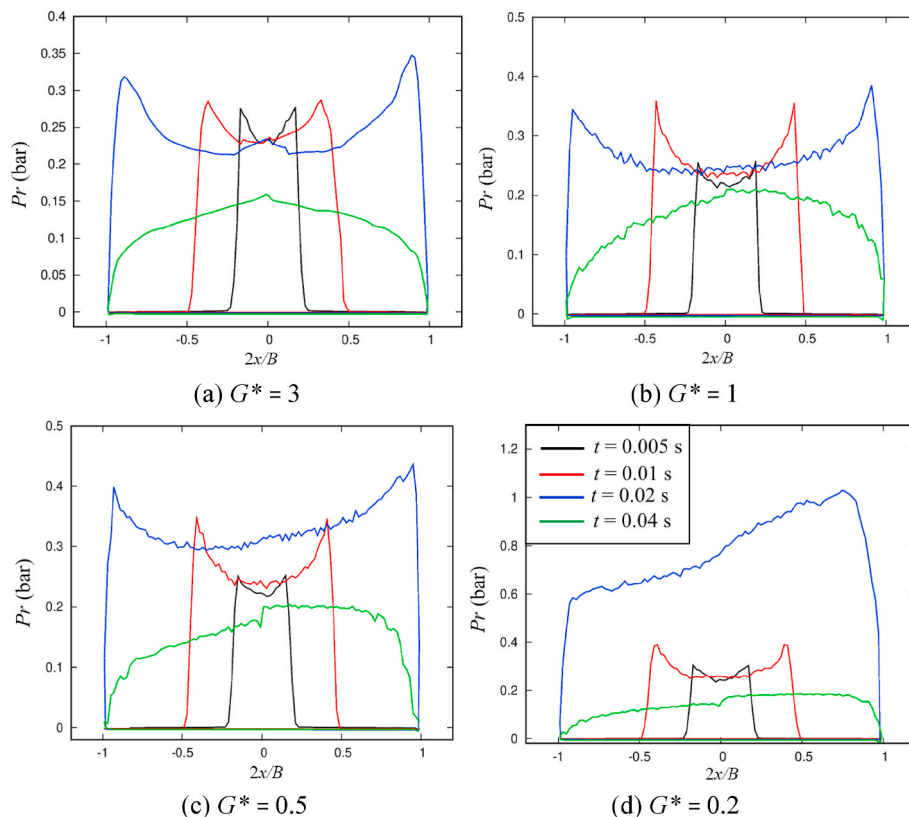

Fig. 18. Pressure distributions on the left wedge at four instants at four gap distances for $V_o = 3.05$ m/s.

symmetric pressure distribution reappears, indicating that the hydrodynamic interaction is subtle. For $G^* = 1$, obvious asymmetric pressure distributions are observed at the entire transition stage. It can be explained that the pressures on the left wedge are significantly affected by the right wedge at such a small distance. The hydrodynamic interaction which can be clearly observed in Figs. 19 and 20 will be discussed later. As the gap narrows from $G^* = 1$ to $G^* = 0.2$, the pressure on the entire wedge nearly triples. However, the enormous pressure distribution only lasts for an extremely short time of milliseconds. Afterwards, the hydrodynamic interaction is weakened, and it imposes very small effects on the pressure distribution.

The flow field are examined in details to investigate the interaction mechanism of twin wedges. Figs. 19 and 20 show the pressure and vertical velocity contours of twin wedges entering water at four moments for $V_o = 3.05$ m/s and $G^* = 0.5$. The units of the pressure and the velocity in the contour legends is Pa and m/s, respectively. When the wedge hits the free surface initially, high impulsive pressure is generated on the wetted surface immediately as shown in Fig. 19(a). Meanwhile, a pair of vortices is generated right above the two apexes of each wedge. The free surfaces are pushed away along two sides of each wedge, see Fig. 20(a), when twin wedges pierce through the free surface. At this moment, the pressures and vortices are approximately symmetric with the center line of each wedge, which is consistent with the symmetric pressure distribution at $t = 0.01$ s in Fig. 18(c). When the wedge is fully wetted, the pressure has a remarkable increase in Fig. 19(b). The maximal force occurs at $t = 0.02$ s in Fig. 12(b), which corresponds to the time when the main flow reaches the knuckles of the wedge. According to the definition of the slamming stage, the occurrence moment of the peak force is the critical moment from the slamming stage into the transition stage. In addition, obvious asymmetric pressure distributions are observed. The pressure contours around the twin wedges are

connected. This indicates that significant hydrodynamic interaction between two wedges occurs. Meantime, the free surfaces are detached from the wedge, and two vortices at the gap are contacted, which forms a bigger vortex, see Fig. 20(b).

As the wedge continues to move downward, the jet flows separated from the twin wedges splash toward the sky. Two jet flows at the gap are contacted and form a cavity on the upper side of the wedge. At this moment, the velocities of the water particles at the gap are relatively small, resulting in the high pressures at the gap in Fig. 19(c). Then, the contraction of the cavity occurs due to the large pressure differences between the inner and the outer sides of the twin wedges. The contraction causes the energy concentration of the cavity. Consequently, the pressure oscillations are generated in Fig. 17(c). The jet flow on the inner side of twin wedges is higher than that on the outer side in Fig. 19 (d). Simultaneously, the vortices accompanying the jet flow shed from the apexes of the wedge successively, see Fig. 20(d). Then, the jet flow at the gap carries a great amount of kinetic energy and strongly reduces the pressures at the gap. It should be noted that the air compressibility, which could not be considered in the present study, may play a significance role in the formation and closure stages of the cavity. However, it is beyond the scope of this study to quantitatively analyze to what extent the air compressibility can affect the pressure, slamming load, and even the behavior of the fluid field.

Further, the effects of the gap distance on the fluid field are discussed in details. Figs. 21 and 22 show the instantaneous pressure and vertical velocity contours around the wedges at two moments for $V_o = 3.05$ m/s and $G^* = 3$. Figs. 23 and 24 show the local fluid field at two moments for $V_o = 3.05$ m/s and $G^* = 1$. Figs. 25–27 show the local fluid field at three moments for $V_o = 3.05$ m/s and $G^* = 0.2$. When twin wedges enter water at the gap distance $G^* = 3$, the hydrodynamic characteristics of each wedge are similar with the case of a single wedge entering water.
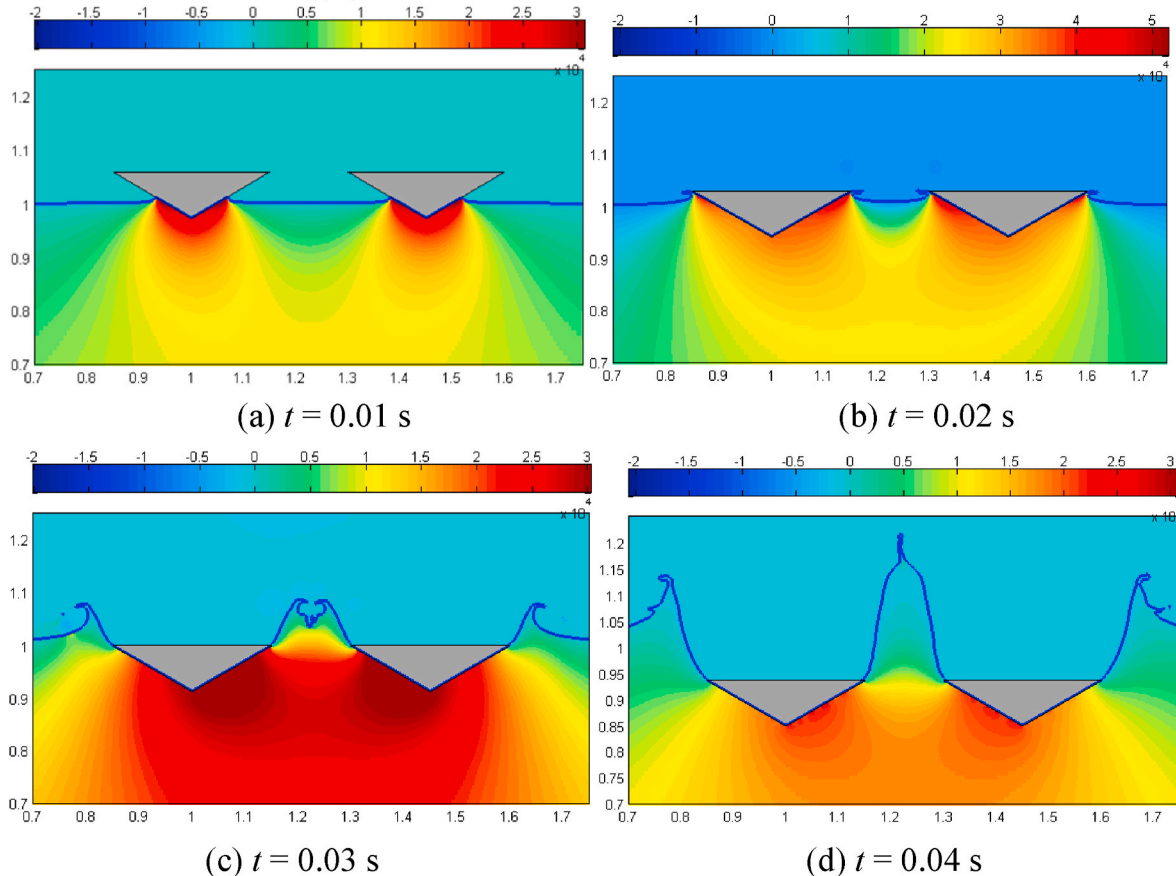

Fig. 19. Instantaneous pressure contours (Pa for the unit of the contour legend) of twin wedges entering water for $V_o = 3.05$ m/s and $G^* = 0.5$ at four moments.
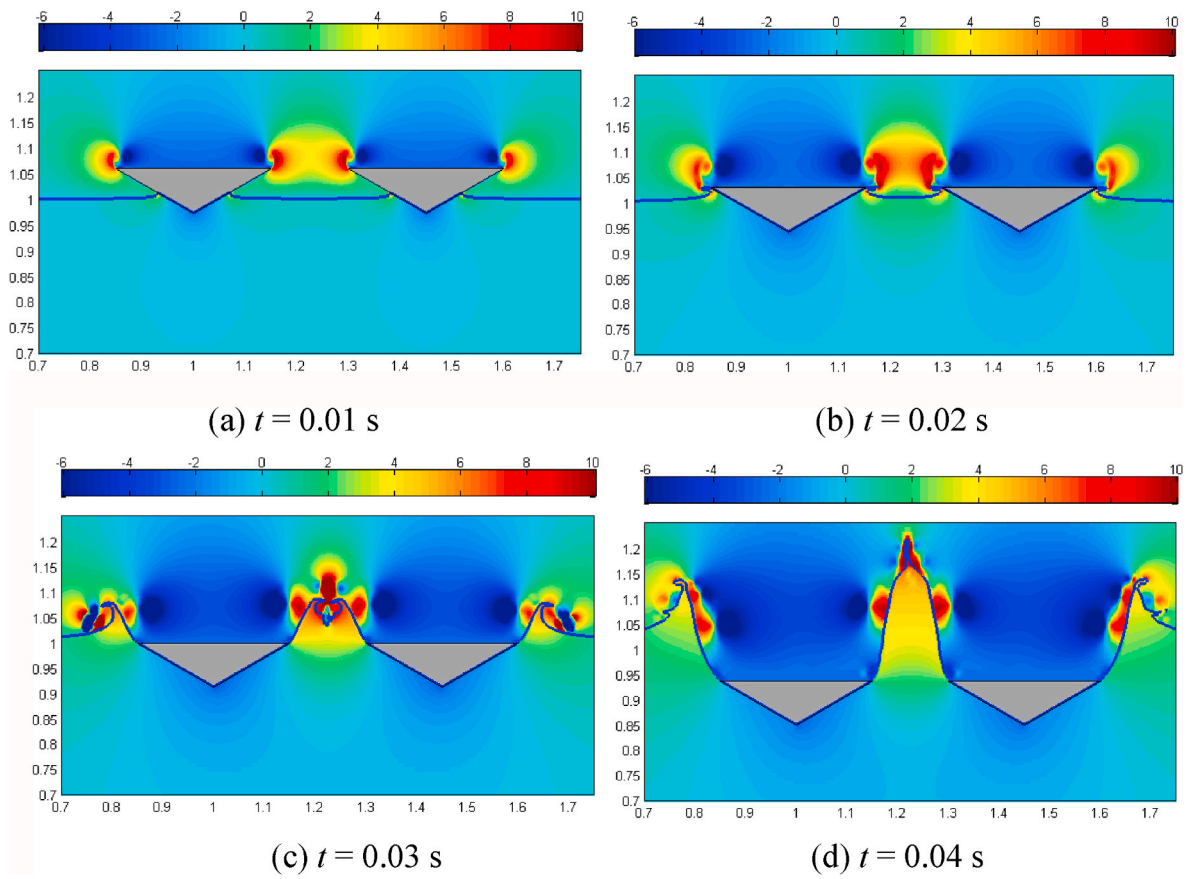
(a) t = 0.01 s

(b) t = 0.02 s

(c) t = 0.03 s

(d) t = 0.04 s

Fig. 20. Instantaneous contours of the vertical velocity (m/s for the unit of the contour legend) for V_o = 3.05 m/s and G^* = 0.5 at four moments.
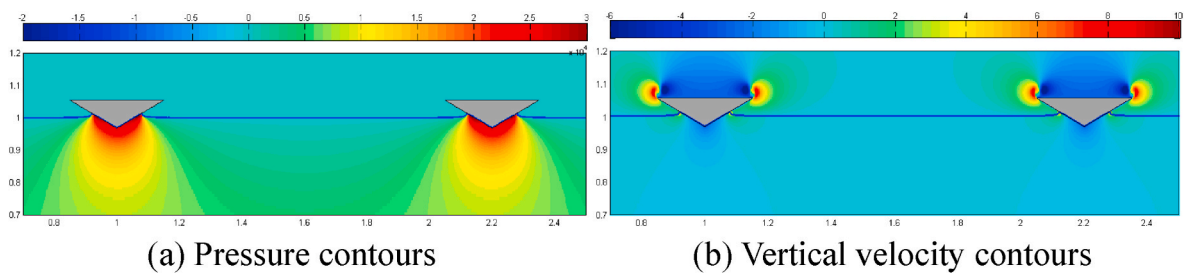

(a) Pressure contours

(b) Vertical velocity contours

Fig. 21. Evolution of twin wedges entering water for V_o = 3.05 m/s and G^* = 3 at t = 0.01 s.

(a) Pressure contours

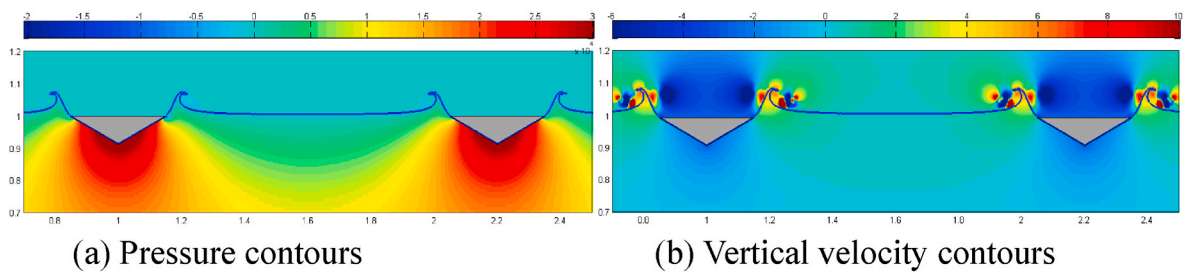(b) Vertical velocity contours

Fig. 22. Evolution of twin wedges entering water for V_o = 3.05 m/s and G^* = 3 at t = 0.03 s.

The pressure and velocity contours are symmetric with the center line of each wedge at the slamming and transition stages, see Figs. 21 and 22. The hydrodynamic interaction between two wedges is not visible, which is confirmed by the symmetric pressure distributions in Fig. 18(a). As the gap narrows to G^* = 1, symmetric pressure contours are observed at the

slamming stage in Fig. 23(a). The obvious hydrodynamic interaction occurs at the transition stage. The pressure contours of twin wedges are connected, and high pressures are accumulated at the gap in Fig. 24(a). Meanwhile, two climbing waves moving to each other form a cavity, accompanying the violent vortex movement at the gap, as shown in
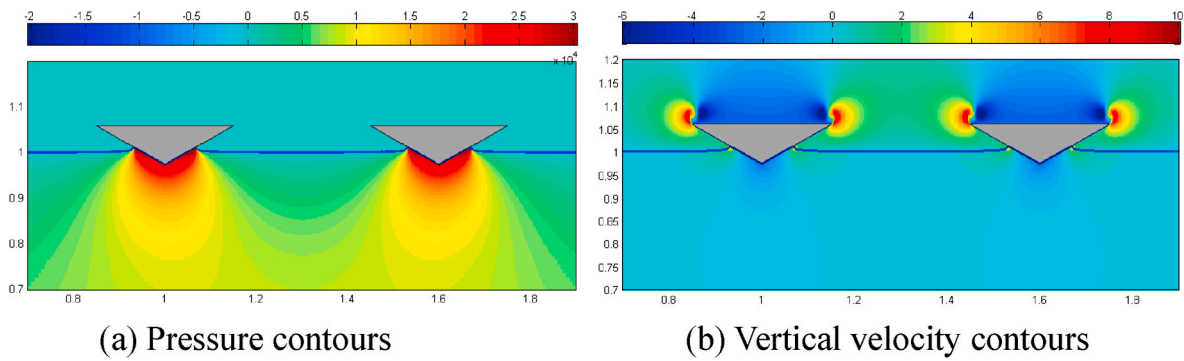
(a) Pressure contours

(b) Vertical velocity contours

Fig. 23. Evolution of twin wedges entering water for $V_o = 3.05$ m/s and $G^* = 1$ at $t = 0.01$ s.

(a) Pressure contours

(b) Vertical velocity contours
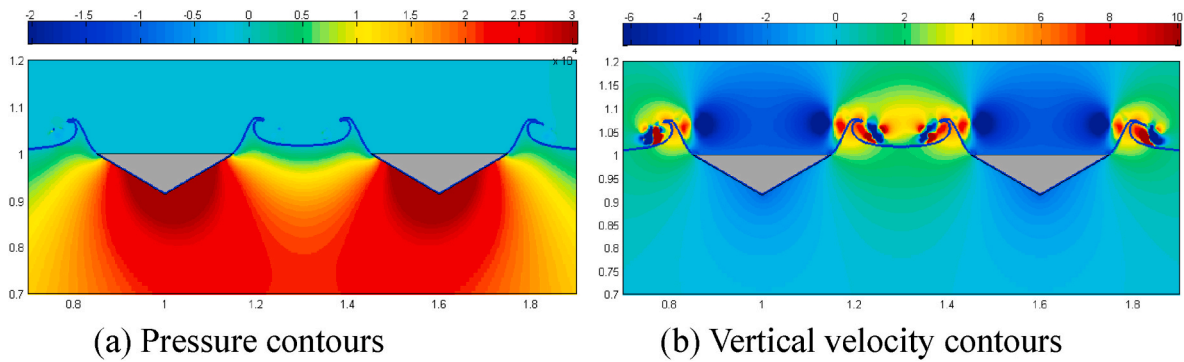
Fig. 24. Evolution of twin wedges entering water for $V_o = 3.05$ m/s and $G^* = 1$ at $t = 0.03$ s.

(a) Pressure contours

(b) Vertical velocity contours

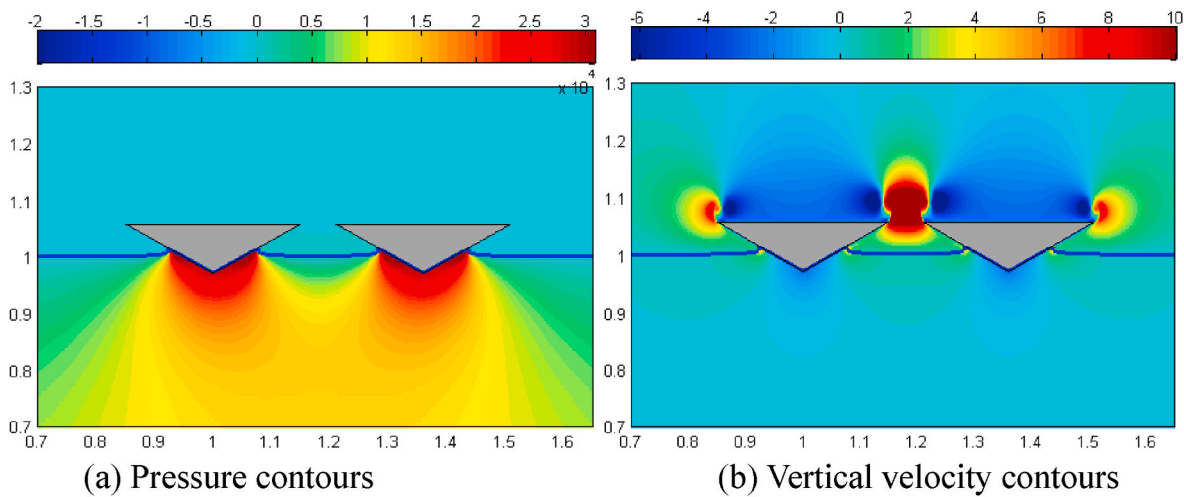**Fig. 25.** Evolution of twin wedges entering water for $V_o = 3.05$ m/s and $G^* = 0.2$ at $t = 0.01$ s.

Fig. 24(b).

When the gap narrows to $G^* = 0.2$, distinct phenomena are observed that the twin wedges behave like a single body. As shown in Fig. 25, the pressure contours are connected, and a big vortex at the gap is generated at the initial stage. As twin wedges move into the water, the water is pushed away. Two climbing waves at the gap reach the knuckles of twin wedges, leading to the forming of a small cavity, as shown in Fig. 26. Simultaneously, extremely high pressures at the gap are generated, which corresponds to the extremely large vertical and horizontal loads in Figs. 12(d) and 13(d). Afterwards, a big jet flow is generated when the cavity is closed in Fig. 27. The jet flow accompanying the big vortices is driven upward by the extremely large pressures, far higher than the jet flows at the outer sides. In the meantime, very thin jet flows at the outer

sides curl up under the effects of the gravity, leading to the forming of the cavities. Also, the negative pressures, that is less than the atmospheric pressure, are observed in the cavity, implying that ventilation can happen.

4. Conclusion and outlook

In this study, a multiphase FSI model based on the Cartesian grid is presented to investigate the water entry of one and twin wedges parametrically. A GALS method is used to capture highly non-linear free surfaces and a RBFGCM method is used to treat arbitrary moving bodies. The mechanism of the hydrodynamic interaction between twin wedges is discussed by systematically analyzing the slamming load, the
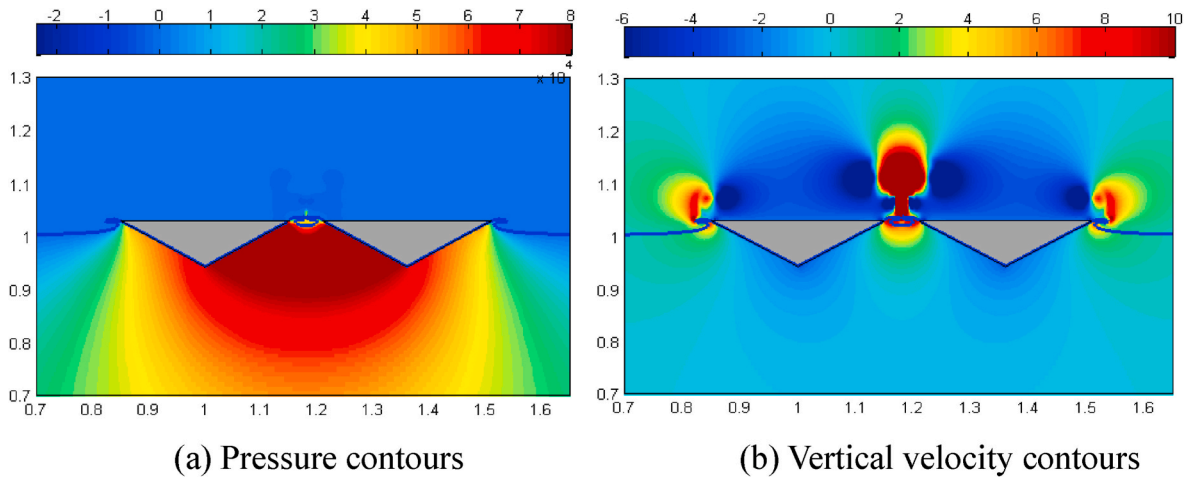
(a) Pressure contours

(b) Vertical velocity contours

Fig. 26. Evolution of twin wedges entering water for $V_o = 3.05$ m/s and $G^* = 0.2$ at $t = 0.02$ s.

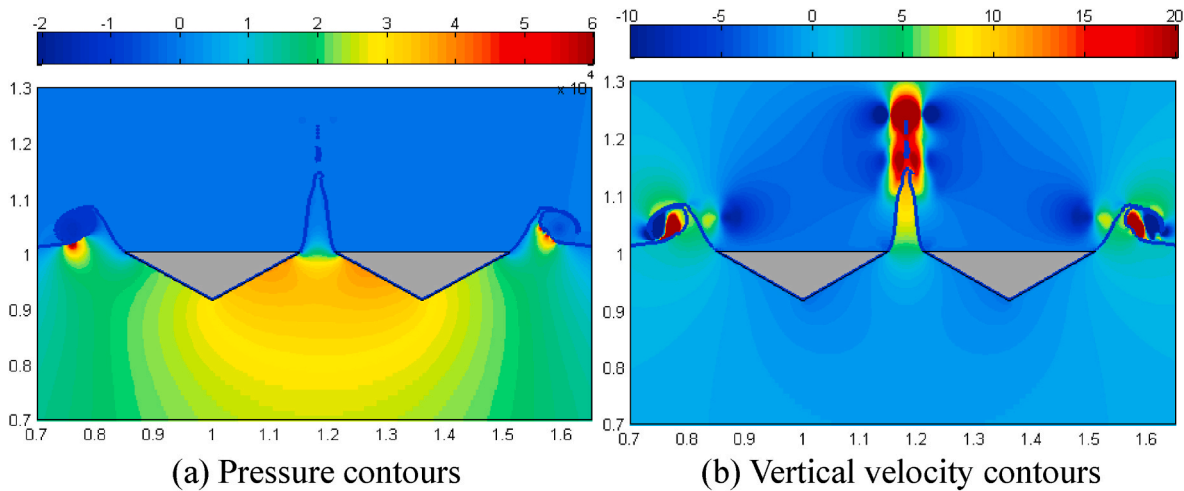(a) Pressure contours

(b) Vertical velocity contours

Fig. 27. Evolution of twin wedges entering water for $V_o = 3.05$ m/s and $G^* = 0.2$ at $t = 0.03$ s.

impulsive pressure, the pressure distribution, and the fluid field under different gap distances and drop velocities. Following conclusions are drawn:

Firstly, a case of twin wedge entering water is simulated to validate the accuracy of the accuracy of the present method. Good convergences on the grid size and the time step are obtained. Then, the water entry of a single free-falling wedge under four drop velocities is simulated. The slamming load and the local pressure agree reasonably with the experimental data and the results of the BEM, confirming the accuracy of the proposed model again. The peak load approximately triples as the drop velocity doubles, while the duration time of the impulsive load is shortened. The peak pressures increase with the rising of the drop velocity, while they are similar at different positions for a given drop velocity. It can be explained that the slamming pressure related to the impact velocity is dominated at the slamming stage, and the impact velocity changes little during the water entry.

Afterwards, the water entry of free-falling twin wedges with various drop velocities and gap distances is simulated. The hydrodynamic interaction between twin wedges is almost negligible for all gap distances at the slamming stage. Significant hydrodynamic interaction is observed for $G^* < 1$ at the transition stage. The small second peak of the vertical load is observed for relatively small gap distances such as $G^* = 0.5$ and $G^* = 1$. As the gap distance narrows to $G^* = 0.2$, the loads and moments of the twin wedges present the single-peak pattern, which is similar to the pattern of a single body entering water. Moreover, the

peak vertical and horizontal loads as well as the moments are over four times than those for $G^* = 0.5$. However, the critical gap distance that twin wedges entering water can be treated as a single body cannot be quantitatively determined since the considered gap distances are limited. Also, the variation patterns of the slamming load and the moment are similar for four drop velocities, indicating that the critical distance may not be affected by the drop velocity. In addition, the horizontal load is approximately one order of magnitude smaller than the vertical forces for various gaps.

The pressure patterns at the transition stage are significantly affected by the hydrodynamic interaction between twin wedges, instead of the drop velocity. The second large pressure pulse at the transition stage is captured for a relatively small gap distance. The pressure pulse is much larger than the slamming pressure when the spray root touches the measuring location, especially for the locations near the knuckle of the wedge. The pressure pulse increases rapidly as the gap distance narrows or the drop velocity rises. However, the pressures at the post-transition stage are almost identical at different positions and gap distances. The reason may be that the slamming pressure reduces dramatically, and the hydrostatic pressure plays an important role.

The evolution of the flow field is also investigated to reproduce the interaction process of twin wedge entering water. The salient phenomena of twin wedge entering water are observed such as the connection of pressure contours, the contact of jet flows, the formation and closure of the cavity, as well as the fusion and split of the vortices. Violent

hydrodynamic interaction occurs for small gap distances such as $G* = 0.5$ when two jet flows at the gap are contacted, forming a cavity. Large pressure differences on the inner and outer side of the cavity cause the contraction and closure of the cavity, leading to a big jet flow. For $G* = 0.2$, the twin wedges behave like a complex single body. A big vortex is generated at the gap. The cavity is formed when the jet flow is separated from the wedge. Also, negative pressures are observed below the curling waves, indicating that the ventilation may happen.

Considering the complexities of the studied problems, multiple degree-of-freedom (DOF) motions are not discussed in the present study, which can be directly simulated by the present numerical method.

CRediT authorship contribution statement

Jianjian Xin: Theory, Methodology, Analysis, and, Writing – original draft. **Fulong Shi:** Theory, Methodology. **Shi Fan:** Writing – review & editing. **Qiu Jin:** Modification, Proofread. **Xing Chang:** Modification, Proofread.

Declaration of competing interest

The authors declare that they have no known competing financial interests or personal relationships that could have appeared to influence the work reported in this paper.

Acknowledgments

References

Aarsnes, J.V., 1996. Drop test with ship sections–effect of roll angle. Marintek Report. (1), 603834.

Bihs, H., Kamath, A., 2017. A combined level set/ghost cell immersed boundary representation for floating body simulations. Int. J. Numer. Methods Fluid. 83, 905–916.

Cheng, Y., Ji, C., Oleg, G., Bai, X., 2018. Wave–current entry of an asymmetric wedge in 3DOF free motions. Eng. Anal. Bound. Elem. 91 (6), 132–149.

Cheng, H., Ming, F.R., Sun, P.N., Sui, Y.T., Zhang, A.M., 2020. Ship hull slamming analysis with smoothed particle hydrodynamics method. Appl. Ocean Res. 101 (4), 102268.

Derakhshanian, M.S., Haghdel, M., Alishahi, M.M., Haghdel, A., 2018. Experimental and numerical investigation for a reliable simulation tool for oblique water entry problems. Ocean Eng. 160, 231–243.

Duan, L., Zhu, L., Chen, M., Pedersen, P.T., 2020. Experimental study on the propagation characteristics of the slamming pressures. Ocean Eng. 217, 107868.

Faltinsen, O.M., 2005. Hydrodynamics of High-Speed Marine Vehicles. Cambridge University, USA.

Hou, Z., Sun, T.Z., Quan, X.B., Zhang, G.Y., Sun, Z., Zong, Z., 2018. Large eddy simulation and experimental investigation on the cavity dynamics and vortex evolution for oblique water entry of a cylinder. Appl. Ocean Res. 81, 76–92.

Hu, Z., Zhao, X., Cheng, D., Zhang, D., 2017. Numerical simulation of water entry of twin wedges using a cip-based method. In: Proceedings of the Twenty-Seventh International Ocean and Polar Engineering Conference, San Francisco, CA, USA. June 25-30.

Hu, Z., Zhao, X., Li, M., Fang, Z., Sun, Z., 2018. A numerical study of water entry of asymmetric wedges using a cip-based model. Ocean Eng. 148 (15), 1–16.

Ji, Z., Xu, F., Takahashi, A., Sun, Y., 2016. Large scale water entry simulation with smoothed particle hydrodynamics on single- and multi-GPU systems. Comput. Phys. Commun. 209, 1–12.

Kim, J., Moin, P., 1985. Application of a fractional-step method to incompressible Navier-Stokes equations. J. Comput. Phys. 59, 308–323.

Kleefsman, K.M.T., Fekken, G., Veldman, A.E.P., Iwanowski, B., Buchner, B., 2005. A volume-of-fluid based simulation method for wave impact problems. J. Comput. Phys. 206 (1), 363–393.

Lee, B.H., Park, J.C., Kim, M.H., Jung, S.J., Ryu, M.C., Kim, Y.S., 2010. Numerical simulation of impact loads using a particle method. Ocean Eng. 37 (2–3), 164–173.

Lee, J., Kim, J., Choi, H., Yang, K.S., 2011. Sources of force oscillations from an immersed boundary method for moving-body problems. J. Comput. Phys. 230, 2677–2695.

Leer, B.V., 1997. Towards the ultimate conservative difference scheme. V-A second-order sequel to Godunov's method. J. Comput. Phys. 32, 101–136.

Li, Y.L., Wan, L., Wang, Y.H., Ma, C.P., Ren, L., 2019. Numerical investigation of interface capturing method by the Rayleigh-taylor instability, dambreak and solitary wave problems. Ocean Eng. 194 (15), 106583.1-106583.16.

Liu, C., Hu, C., 2014. An efficient immersed boundary treatment for complex moving object. J. Comput. Phys. 274, 654–680.

Lu, L., Teng, B., Sun, L., Chen, B., 2011. Modelling of multi-bodies in close proximity under water waves-Fluid forces on floating bodies. Ocean Eng. 38 (13), 1403–1416.

Mahmoodi, M., Shademani, R., Gorji-Bandpy, M., 2018. Viscous models comparison in water impact of twin 2d falling wedges simulation by different numerical solvers. Int. J. Market. Technol. 9, 1–13.

Miloh, T., 1991. On the oblique water-entry problem of a rigid sphere. J. Eng. Math. 25 (1), 77–92.

Mohaghegh, F., Udaykumar, H.S., 2016. Comparison of sharp and smoothed interface methods for simulation of particulate flows I: fluid structure interaction for moderate Reynolds numbers. Comput. Fluids 140, 39–58.

Nave, J.C., Rosales, R.R., Seibold, B., 2010. A gradient-augmented level set method with an optimally local, coherent advection scheme. J. Comput. Phys. 229 (10), 3802–3827.

Nguyen, V., Park, W., 2016. A free surface flow solver for complex three-dimensional water impact problems based on the VOF method. Int. J. Numer. Methods Fluid. 82 (1), 3–34.

Shabani, B., Lavroff, J., Davis, M.R., Holloway, D.S., Thomas, G.A., 2019. Slam loads and pressures acting on high-speed wave-piercing catamarans in regular waves. Mar. Struct. 66 (7), 136–153.

Shademani, R., Ghadimi, P., 2017. Parametric investigation of the effects of deadrise angle and demi-hull separation on impact forces and spray characteristics of catamaran water entry. J. Braz. Soc. Mech. Sci. Eng. 39 (6), 1989–1999.

Shi, F., Xin, J., Jin, Q., 2019. A Cartesian grid based multiphase flow model for water impact of an arbitrary complex body. Int. J. Multiphas. Flow 110, 132–147.

Sotiropoulos, F., Yang, X., 2014. Immersed boundary methods for simulating fluid–structure interaction. Prog. Aero. Sci. 65 (5), 1–21.

Sun, H., 2007. A Boundary Element Method Applied to Strongly Nonlinear Wave-Body Interaction Problems. Ph.D. Dissertation. Department of Marine Technology.

Sun, H., Faltinsen, O.M., 2009. Water entry of a bow-flare ship section with roll angle. J. Mar. Sci. Technol. 14 (1), 69–79.

Sun, S.L., Wu, G.X., 2014. Fully nonlinear simulation for fluid/structure impact: a review. J. Mar. Sci. Appl. 13, 237–244.

Sun, Z., Jiang, Y.C., Zhang, G.Y., Zong, Z., Xing, J.T., Djidjeli, K., 2019. Slamming load on trimaran cross section with rigid and flexible arches. Mar. Struct. 66 (7), 227–241.

Sun, Z., Korobkin, A., Sui, X.P., Zhi, Z., 2021. A semi-analytical model of hydroelastic slamming. J. Fluid Struct. 101, 103200.

Van der Vorst, H.A., 2003. Iterative Krylov Methods for Large Linear Systems. Cambridge University Press.

Von Karman, T., 1929. The Impact of Seaplane Floats during Landing. National Advisory Committee for Aeronautics, Washington, USA, October. NACA TN 321.

Wang, J., Lugni, C., Faltinsen, O.M., 2015. Experimental and numerical investigation of a freefall wedge vertically entering the water surface. Appl. Ocean Res. 51, 181–203.

Wang, K., Ma, X., Bai, W., Lin, Z., Li, Y., 2021. Numerical simulation of water entry of a symmetric/asymmetric wedge into waves using openfoam. Ocean Eng. 227 (3), 108923.

Wang, L., Xu, F., Yang, Y., 2019. Sph scheme for simulating the water entry of an elastomer. Ocean Eng. 178 (15), 233–245.

Wu, G.X., 2006. Numerical simulation of water entry of twin wedges. J. Fluid Struct. 22, 99–108.

Xia, W., Wang, C., Wei, Y.J., Li, J., 2019. Experimental study on water entry of inclined circular cylinders with horizontal velocities. Int. J. Multiphas. Flow 118, 37–49.

Xie, F., Qu, Y., Islam, M.A., Meng, G., 2020. A sharp-interface cartesian grid method for time-domain acoustic scattering from complex geometries. Comput. Fluids 202, 104498.

Xie, H., Liu, F., Yu, P., Ren, H., 2019. Comparative study on fluid dynamic behavior and slamming loads of two bow-flare sections entering into water. Int. J. Mech. Sci. 166 (8), 105177.

Xie, H., Liu, F., Yu, P., Ren, H., 2020. Numerical simulation on the water entry of bow-flare section considering bulbous bow. Ocean Eng. 205 (4), 107081.

Xie, H., Ren, H., Li, H., Tao, K., 2018. Numerical prediction of slamming on bow-flared section considering geometrical and kinematic asymmetry. Ocean Eng. 158, 311–330.

Xin, J., Shi, F., Jin, Q., Lin, C., 2018. A radial basis function based ghost cell method with improved mass conservation for complex moving boundary flows. Comput. Fluids 176 (15), 210–225.

Yang, J.M., 2016. Sharp interface direct forcing immersed boundary methods: a summary of some algorithms and applications. J. Hydrodyn. 5 (28), 5–22.

Yousefnezhad, R., Zeraatgar, H., 2014. A parametric study on water-entry of a twin wedge by boundary element method. J. Mar. Sci. Technol. 19 (3), 314–326.

Zhang, Y., 2010. A level set immersed boundary method for water entry and exit. Commun. Comput. Phys. 8 (2), 265–288.

Zhao, R., Faltinsen, O., 1993. Water entry of two-dimensional bodies. J. Fluid Mech. 246 (-1), 593–612.

Zhao, R., Faltinsen, O., Aarsnes, J., 1996. Water entry of arbitrary two-dimensional sections with and without flow separation. In: Proceedings of the 21st Symposium on Naval Hydrodynamics. Trondheim, Norway. National Academy Press, Washington, DC, USA, pp. 408–423.

Zheng, K.Y., Zhao, X.Z., Yan, D.M., 2020. Numerical simulation of water entry of two-dimensional structures with complex geometry using a cip-based model. Appl. Ocean Res. 102379.